Facet-specific reactivity of hematite nanocrystals during Fe (II)-catalyzed recrystallization

Fei Wu [a,b,c], Jian Hua [b], Jimei Zhou [a,c], Yuhui Liu [a,c], Shengqiao Long [a,c], Yingheng Fei [d,*], Chengshuai Liu [a,b,**]

[a] *State Key Laboratory of Environmental Geochemistry, Institute of Geochemistry, Chinese Academy of Sciences, Guiyang 550081, PR China*
[b] *National-Regional Joint Engineering Research Center for Soil Pollution Control and Remediation in South China, Guangdong Key Laboratory of Integrated Agro-environmental Pollution Control and Management, Institute of Eco-environmental and Soil Sciences, Guangdong Academy of Sciences, Guangzhou 510650, PR China*
[c] *University of Chinese Academy of Sciences, Beijing 100049, PR China*
[d] *School of Environmental Science and Engineering, Guangzhou University, Guangzhou 510006, PR China*

ABSTRACT

Hematite (α-Fe$_2$O$_3$) surfaces represent one of the most common redox-active interfaces in the environment, playing an important role in the biogeochemical cycling of metal elements in the subsurface. Fe(II)-catalyzed recrystallization of iron (hydr)oxides is a fundamental process of iron cycling in earth's surface environments, but the proposed Fe(II)$_{aq}$-Fe(III) electron transfer and Fe atom exchange mechanism of recrystallization remains poorly understood at the atomic level. Here, two different structurally well-defined single crystals of hematite were employed to react with Fe(II)$_{aq}$ at neutral pH. Compared with hematite nanoplates (HNPs) exposed with {001} facets, hematite nanocubes (HNCs) exposed with {012} facets displayed higher adsorption capacity for Fe(II)$_{aq}$ and underwent more Fe atom exchange, indicating the Fe(II)-catalyzed recrystallization process relied on exposed facets of hematite. Hematite recrystallization caused suppression on Morin transition and increase in crystallinity for both HNCs and HNPs, with the extent depending on surface structure. Density functional theory calculations revealed that the facet-specific differences were directly linked with the density of surface Fe atoms and their coordination conditions. The findings highlight the important roles of surface structure of iron (hydr) oxides in the Fe(II)-catalyzed recrystallization, and provide fundamental data to iron atom exchange, suggesting that the surface structure sensitivity should be considered to estimate the reactivity at the mineral-liquid interface.

1. Introduction

Hematite (α-Fe$_2$O$_3$) is widespread throughout the Earth's near-surface environment at both the nano- and macroscopic scales (Cornell and Schwertmann, 2003). Naturally occurring hematite particles exhibit different morphologies and sizes and range from well-defined platy crystals to more spherical shapes, depending on the physical and/or geochemical conditions during mineral formation and subsequent dissolution (Carbone et al., 2005; Echigo et al., 2012). The different particle morphologies result in a different proportion of crystallographic facets, such as the (001), (012), and (110) facets (Venema et al., 1998). As a key feature controlling the coordination of the surface metal atoms, the exposed facets and their surface-active site density can strongly influence the reactivity at the hematite/solution interfaces in many processes that rely on interfacial electrostatics, such as heavy-metal-ion adsorption (Huang et al., 2016a; Noerpel et al., 2016; Yuan et al., 2017; Huang et al., 2019a; Liang et al., 2019; Lounsbury et al., 2019; Jiang et al., 2020; Mei et al., 2020), catalytic performance (Zhou et al., 2012; Chan et al., 2015; Huang et al., 2016b; Sun et al., 2018; Cao et al., 2019; Huang et al., 2019a; Li et al., 2020; Guo et al., 2021), and interfacial electron transfer (Catalano et al., 2010; Joshi et al., 2017; Huang et al., 2018). Therefore, understanding the interfacial redox reactivity of hematite facets is of great importance for the accurate conceptualization of a series of phenomena, such as the biogeochemical cycling of trace elements and contaminants and the reductive dissolution and oxidative growth of iron (hydr)oxides.

The interaction between Fe(II)$_{aq}$ and iron (hydr)oxides in anoxic environments, commonly referred to as Fe(II)-catalyzed recrystallization (Handler et al., 2009; Frierdich et al., 2015; Joshi and Gorski, 2016; Joshi et al., 2017), is a universal and important reaction in iron cycling and has a significant impact on the groundwater quality, contaminant remediation, and biogeochemical cycling of metals (Joshi et al., 2017). Based on ^{57}Fe isotope experiments, Fe atom exchange occurs between the Fe(III) in hematite's structure and Fe(II)$_{aq}$, without overt changes to the structure of hematite (Larese-Casanova and Scherer, 2007a; Larese-Casanova and Scherer, 2007b; Rosso et al., 2010; Frierdich et al., 2015). Additionally, ^{57}Fe Mössbauer spectroscopy studies have confirmed that the adsorbed Fe(II) is oxidized to Fe(III) via interfacial electron transfer with the underlying hematite (Larese-Casanova and Scherer, 2007a; Larese-Casanova and Scherer, 2007b; Rosso et al., 2010; Frierdich et al., 2015). These studies also indicated that the sorption of Fe(II), followed by interfacial electron exchange, alters the bulk magnetic properties of hematite (Larese-Casanova and Scherer, 2007a; Larese-Casanova and Scherer, 2007b; Rosso et al., 2010; Frierdich et al., 2015).

However, to date, most studies were conducted using fine-grained oxide materials with uncontrolled or uncharacterized particle shapes and/or surface characteristics, making it difficult to investigate the underlying structure-specific mechanisms of the Fe(II)-catalyzed recrystallization process at the molecular and/or atomic levels. There are also some studies using hematite microparticles (generally exposed with basal (001) and edge facets) to explore the facet-selective adsorption of Fe(II)$_{aq}$. For example, in a study of Fe(II)$_{aq}$ interactions with single crystals of hematite, it was found that the oxidative adsorption of Fe(II) onto the (001) basal plane was coupled with the simultaneous dissolution of the edge surfaces (Yanina and Rosso, 2008). Studies involving X-ray reflectivity (XRR) (Catalano et al., 2010), second harmonic generation (Jordan et al., 2013), and crystal truncation rod (CTR) (Tanwar et al., 2008; Tanwar et al., 2009) have revealed that Fe(II) alters the surface of hematite and consequently affects the oxidation efficiency of Fe(II) by the lattice Fe(III). Models fit with XRR (Catalano et al., 2010) and CTR (Mackrodt et al., 1987; Tanwar et al., 2008; Tanwar et al., 2009) datasets also suggest that the interfacial roughness and/or termination of the (012) and (110) facets change in a manner distinct from that of the (001) facet. These studies have demonstrated that the reaction of Fe(II)$_{aq}$ with hematite causes surface structural changes, and this reaction is controlled by both the bulk and surface structures of the hematite. These studies provide valuable information on the structure and reactivity of individual facets, however, they did not take the recrystallization process into account, such as extent of Fe atom exchange and changes to the hematite structure and magnetic property. There was only one study examined the effects of different particle morphologies of hematite on the Fe(II)-catalyzed recrystallization process, which was looking at differences in surface area specifically, not necessary facet-specific differences (Frierdich et al., 2015).

The objective of this study is to understand the facet-dependent effects of hematite in mediating the Fe(II)-catalyzed recrystallization process. To achieve this objective, we obtained two types of well-defined hematite nanocrystals with predominantly exposed {012} and {001} facets. The hematite {001} and {012} facets were selected because they are the most commonly and naturally growing planes and are responsible for most reaction processes involving hematite (Mackrodt et al., 1987). Then, ^{57}Fe(II)$_{aq}$ adsorption experiments were conducted to explore the affinities for the surface sites of hematite with different exposed facets. Changes in the structure, magnetic property, and oxidation state of hematite during Fe(II)-catalyzed recrystallization were examined using Rietveld refinements, high-resolution transmission electron microscopy (HR-TEM), and Mössbauer spectroscopy. Finally, density function theory (DFT) calculations were conducted to determine the atomic surface structures and corresponding binding geometries. Based on the experimental and simulation results, we propose that the Fe(II)-catalyzed recrystallization process may be correlated with the coordination conditions of the Fe on the hematite surfaces.

2. Materials and methods

2.1. Chemicals and materials

All of the chemicals used in this study were of analytical grade and were used without further purification. The deionized water (18.2 MΩ) was prepared using an ultrapure water system (Milli-Q Reference A+, Merck Millipore, France) and was used throughout the experiments.

2.2. Hematite nanoparticles synthesis and characterization

Hematite nanocubes (HNCs) with predominantly exposed {012} facets were prepared by adapting the procedure used in a previous study (Wang et al., 2007). Briefly, 4.3 mL of oleic acid, 6.93 g of sodium oleate, and 35 mL of ethanol were mixed thoroughly at room temperature by stirring. After this, 2.08 g of FeCl$_3$·6H$_2$O was added, and the solution was stirred for 30 min. The mixed reactant was then transferred into a 100 mL Teflon-lined stainless-steel autoclave and was heated in an oven at 180 °C for 10 h. Hematite nanoplates (HNPs) with predominantly exposed {001} facets were synthesized according to previously reported methods (Chen et al., 2010; Huang et al., 2017b). Briefly, 1.09 g of FeCl$_3$·6H$_2$O was dissolved by vigorously stirring in 40.0 mL of ethanol with 2.8 mL of DI water. After this, 3.2 g of sodium acetate was added while stirring. The mixture was then sealed in a 100 mL Teflon-lined stainless-steel autoclave and heated in an oven at 180 °C for 12 h. Both the precipitates were collected and washed thoroughly with deionized water and ethanol, dried in an oven at 60 °C overnight, and passed through a 100-mesh sieve. To remove the residual organic solvent on the surface of hematite, the obtained materials were calcined in air at 400 °C for 2 h following the methods that reported previously (Lv et al., 2018). It should be noted that the calcination may decrease the reactivity of iron (hydr)oxides toward Fe(II)$_{aq}$, however, it can also remove surface defects of iron (hydr)oxides (Notini et al., 2018; Notini et al., 2019), which is helpful to compare the reactivity of different facets of hematite. After naturally cooling to room temperature, the hematite powders were collected for use. The details of the characterization techniques and DFT calculations are described in the Supplementary Information (SI) (Characterization of Hematite Nanoparticles: Text S1; DFT Calculations: Text S2).

2.3. Iron isotope exchange experiments

Isotope exchange reactions were conducted using natural isotopic abundance hematite (^{NA}hematite) and ^{57}Fe(II)$_{aq}$. All of the exchange experiments were carried out in an anoxic glovebox (92% N$_2$, 8% H$_2$) with a Pd catalyst removing any traces of oxygen. All of the solutions were purged with N$_2$ for at least 3 h prior to being taken into the glovebox (Coy Lab Products Inc., MI), and exposed to the anoxic atmosphere in the chamber for at least 48 h before the experiments. The ^{57}Fe enriched 0.1 M Fe(II)$_{aq}$ stock solution was prepared by dissolving ^{57}Fe (0) powder (^{57}Fe > 96%, Isoflex) in warm (70 °C) 5 M HCl in a glass vial, and it was stored in the anoxic glovebox. Batch reactors were prepared by adding 10 mL of 25 mM HEPES buffer adjusted to a pH of 7.5 ± 0.02 and 25 mM KBr electrolyte to a 15 mL polypropylene centrifuge tube and adding 10 μL of ^{57}Fe(II) stock to create an aqueous Fe(II) solution with a concentration of 1 mM. It should be noted that the use of a buffer may affect the reaction between Fe(II)$_{aq}$ and hematite; however, since it was necessary to maintain a constant pH, the HEPES buffer was chosen according to previous studies conducted under similar conditions (Frierdich et al., 2014; Handler et al., 2014; Frierdich et al., 2015). After equilibrating for 2 h, the batch reactors were filtered into new tubes using 0.22 μm nylon syringe tip filters. An aliquot was used to determine the initial Fe(II) concentration, and the experiments were started by adding 20.0 ± 0.2 mg of hematite nanoparticles to produce a solution of 2 g·L^{-1} hematite. The reactors were wrapped in Al-foil and were continuously mixed on an end-over-end rotator in the dark. The control

experiments were performed using the same method but without ^{57}Fe (II), and the solids were collected for phase characterization after the suspensions were centrifuged and filtered. Samples were reacted for 60 days to ensure the complete adsorption-desorption equilibrium was reached.

After time periods ranging from 3 h to 60 days, the iron concentrations and Fe isotope compositions of the reactors were analyzed as follows. (1) Fe(II)$_{aq}$ was isolated by centrifuging each reactor and filtering the supernatant (0.22 μm) into a new tube in which the sample was acidified with 50 μL of 5 M HCl. (2) Then, the Fe(II) adsorbed on hematite (Fe(II)$_{extr}$) was recovered by resuspending the solid in the original reactor for 15 min in 10 mL of 0.4 M HCl. This suspension was then centrifuged and the supernatant was filtered into a clean sample tube. (3) The residual solid in the original reactor was completely dissolved in 5 mL of 5 M HCl to determine the total amount of solid Fe. The Fe(II) concentrations of these three sample fractions were quantified using the phenanthroline method (Stookey, 1970). The total Fe was determined after reduction of the Fe(III) using hydroxylamine hydrochloride, and the Fe(III) was calculated as the difference between the total Fe and the Fe(II).

2.4. Fe isotope analyses

The iron isotope analyses were carried out using a PerkinElmer NexION 300D inductively coupled plasma mass spectrometer (ICP-MS). The polyatomic argide molecules (e.g., ^{56}[ArO]$^+$ and ^{54}[ArN]$^+$) were removed using a collision cell gas containing a He:H$_2$ mixture of 93%:7% (Frierdich et al., 2015). All of the solutions were diluted with 2% HCl (trace metal grade) to obtain an Fe concentration of ~0.5 μM prior to analysis. The iron isotope fractions (*f*) were calculated by dividing the counts in each isotope channel by the sum of the total counts of all four channels (i.e., ^{54}Fe, ^{56}Fe, ^{57}Fe, and ^{58}Fe). The *f* ^{57}Fe values of the Fe(II)$_{aq}$ were used to calculate the relative amount of Fe atoms in hematite nanoparticles that exchanged with the Fe(II)$_{aq}$ according to the following equation (Handler et al., 2014; Frierdich et al., 2015):

$$\text{Fe atom exchange } (\%) = \frac{N_{aq} \times \left(f_{aq}^i - f_{Fe(II)}^t \right)}{N_{Hem}^{Tot} \times \left(f_{Fe(II)}^t - f_{hem}^i \right)} \times 100 \qquad (1)$$

where N_{aq} is the number of moles of Fe(II)$_{aq}$ in the solution; N_{Hem}^{Tot} is the total number of moles of Fe in the hematite; f_{aq}^i is the initial isotopic fraction of Fe(II)$_{aq}$; f_{hem}^i is the initial isotopic fraction of hematite; and $f_{Fe(II)}^t$ is the isotopic fraction of Fe(II)$_{aq}$ at reaction time *t*.

3. Results and discussion

3.1. Structural differences between HNCs and HNPs

The obtained powder X-ray diffraction (XRD) patterns (Fig. S1a) of hematite nanoparticles matched with a rhombohedral hexagonal phase (α-Fe$_2$O$_3$, JCPDS No. 99–0060). No peaks for other phases were observed, confirming that the prepared hematite samples were pure and highly crystalline. It should be noted that the strongest peaks of HNCs and HNPs were the (104) and (110) peaks, respectively. The mean crystallite dimension (MCD) (104) was used to represent the crystal size along the *c*-axis, while the MCD (110) was used to represent that of the *a*-*b* plane. These results indicate that the HNCs exhibited better crystal development than the HNPs in the *c* direction (Cornell and Schwertmann, 2003; Chan et al., 2015). These characteristics are in well accordance with previous studies (Chan et al., 2015; Huang et al., 2019a; Li et al., 2020), suggesting the successful preparation of hematite with different exposed facet. The corresponding Raman spectra are shown in Fig. S2b. The bands centered at 219.0, 240.0, 286.7, 401.7, 492.7, and 603.3 cm^{-1} were assigned to the A$_{1g}$(1), E$_g$(1), E$_g$(2), E$_g$(3),

A$_{1g}$(2), and E$_g$(4) vibration modes, respectively (Qu et al., 2013). The A$_{1g}$ peaks are the antisymmetric stretching and bending vibrations of the O-Fe-O in α-Fe$_2$O$_3$; and the E$_g$ peaks are the symmetric stretching vibrations of the O-Fe-O (Yan et al., 2020). Notably, the relative intensity of the A$_{1g}$ peak of HNCs was higher than that of HNPs, while the relative intensity of the E$_g$ peak was lower, due to their different O–Fe–O atomic structures. Specifically, HNCs possesses 100% 5-fold under-coordination (Fe$_{5c}$) sites, while HNPs facet has a single iron-layer with 100% 3-fold under-coordination (Fe$_{3c}$) sites (Fig. 2). As is shown in Fig. S2, the peaks of NaAc are located at 166 and 667 cm^{-1}; however, these peaks are not obvious in the hematite nanoparticles, which indicates that there is no significant acetate residue (Zong et al., 2021). The hematite nanoparticles had similar specific surface areas, specifically 40.7 and 41.3 m^2·g^{-1} for HNCs and HNPs (Table 1), respectively, which facilitates the comparison of their reactivity toward Fe(II)$_{aq}$.

The scanning electron microscopy (SEM) results (Fig. S3) demonstrate that the prepared HNCs and HNPs were dispersed as individual particles with uniform pseudocubes and hexagonal plates, respectively. HNCs had a mean side length of 30.3 nm based on the transmission electron microscopy (TEM) images (Fig. 1a). By taking the HR-TEM image of a single pseudocube from the top (Fig. 1b), three sets of lattice fringes were observed with interplanar distances of 0.37 nm, 0.37 nm, and 0.25 nm. Furthermore, the dihedral angles of the two exposed adjacent planes were 86° or 94°. These structural features are highly consistent with the hematite (012) and (1$^-$02) planes (see the corresponding fast-Fourier transform (FFT) patterns in Fig. 1c). Similarly, the front, side, and top surfaces of the pseudocube corresponded to the (012), (1$^-$02), and (11$^-$2) planes, respectively. The relationships between these facets are schematically illustrated in Fig. 1d. The hidden planes of the pseudocube (Fig. 1c) were (01$^-$2), (102$^-$), and (1$^-$12$^-$). Therefore, HNCs was completely exposed with {012} facets (Ouyang et al., 2014; Huang et al., 2019a). The average diameter and thickness of HNPs were 74.3 and 14.5 nm, respectively (Fig. 1e and i). The HR-TEM images (Fig. 1f) and FFT patterns (Fig. 1g) revealed two sets of lattice fringes, each separated by 0.25 nm. Based on this and the intersection angle of 60°, these lattice fringes were assigned to the (110), (2$^-$10), and (1$^-$20) planes. Consequently, the basal top and bottom surfaces were unambiguously confirmed to be the {001} planes. From the side view of the nanoplates (Fig. 1i), the stacks along the {001} facet, likely a result of drying during drop-casting on the TEM grid, was typical (Chan et al., 2015; Huang et al., 2016a; Huang et al., 2019a). Fig. 1j shows a side view of a nanoplate particle, and the distinguishable 0.25 and 0.46 nm lattice fringes are consistent with (110) and (003) planes, in the high-resolution TEM images, which is confirmed by the corresponding FFT pattern (Fig. 1k). Therefore, the HNPs was enclosed by two {001} basal planes and six {012} side planes (Ouyang et al., 2014; Huang et al., 2016a; Zong et al., 2021), with the {012} surface facets occupying ~18.4% of the total surface area based on a simple estimation based on the average diameter and thickness of the nanoplates. Schematic drawings of the HNPs shapes and plane indices are shown in Fig. 1h and l, respectively.

The surface iron oxidation states and the surface species on the different facets were determined via X-ray photoelectron spectroscopy (XPS). In the Fe 2p region (Fig. S1b), no obvious difference was observed between HNCs and HNPs. The Fe 2p$_{3/2}$ and 2p$_{1/2}$ peaks were located at around 710.5 eV and 724.1 eV, respectively, which is in agreement with the reported values for Fe^{3+} (Zhou et al., 2010; Zhou et al., 2012; Ouyang et al., 2014). The additional satellite peaks (e.g., 719.2 and 732.8) are attributed to charge transfer (Norgren et al., 1994; Descostes et al., 2000) and/or to shake-up processes (Baltrusaitis et al., 2007). In the O 1 s region (Fig. S1c and d), the broad O 1 s peak can be deconvoluted into three distinct peaks that correspond to chemisorbed OH species, lattice OH species, and lattice O^{2-} species (Baltrusaitis et al., 2007). By comparing the relative areas of the deconvoluted peaks, the relative percentages of the surface oxygen atoms in the surface hydroxyl sites were determined to be about 33.5% and 29.3% for HNCs and HNPs,

Table 1

Physicochemical properties of HNCs and HNPs.

Sample	SSA[a] ($m^2 \cdot g^{-1}$)	q[b] ($\mu mol \cdot g^{-1}$)	Γ[c] (#Fe·nm^{-2})	Exposed facets	Surface area ratio (%)	Facet Γ (#Fe·nm^{-2})	Hem Fe Ex[d] (%)
HNCs	40.7	150.8	2.23	{012}	100	2.23	5.2
HNPs	41.3	101.3	1.48	{001}	81.6	1.70	3.0
				{012}	18.4	2.23	

[a] The specific surface (SSA) was determined by N_2 adsorption-desorption of hematite nanoparticles.

[b] Calculated from the average of the last three $Fe(II)_{aq}$ concentration time points minus the initial $Fe(II)_{aq}$ concentration.

[c] $\Gamma = (Q \times 10^{-6} \times 6.02 \times 10^{23})/(SSA \times 10^{18})$.

[d] Taken as the average of the last three time point for each reaction.
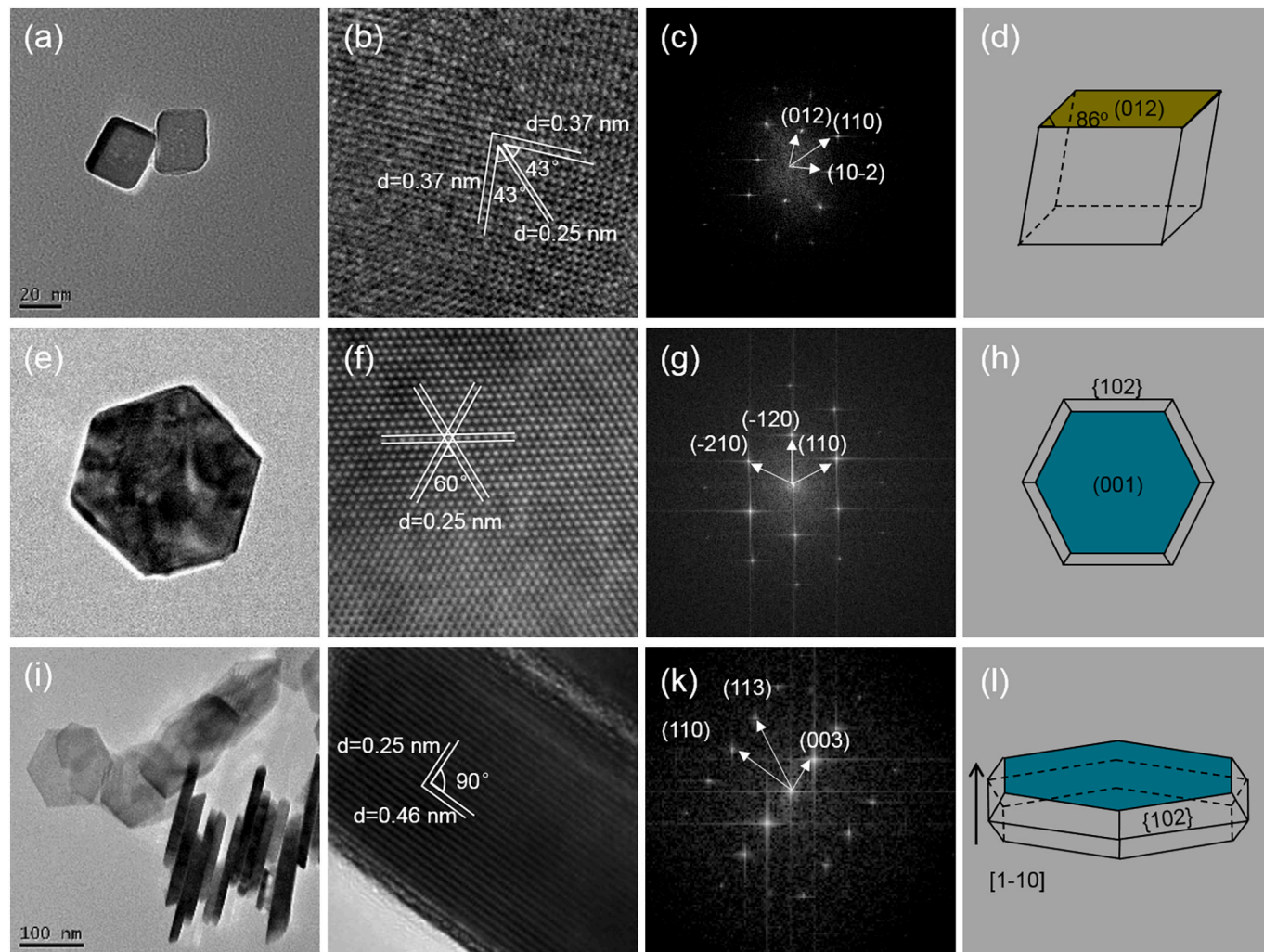

Fig. 1. Representative morphologies crystalline and structure of hematite nanoparticles. (a) TEM image, (b) high-resolution TEM image, (c) FFT pattern, (d) schematic drawing of HNCs, (e) TEM image, (f) high-resolution TEM image, (g) FFT pattern, (h) schematic drawing of top-view of HNPs, (i) TEM image, (j) high-resolution TEM image, (k) FFT pattern, and (l) schematic drawing of side-view of HNPs.

respectively (Table S1). The above analysis indicates that the HNCs and HNPs possessed different surface structures, and thus, they could be expected to have different adsorption capacities for metal ions.

The magnetic properties of hematite nanoparticles were assessed via Mössbauer spectroscopy at room temperature (298 K) and 13 K (Fig. S4). The spectra exhibit the characteristic sextet of high-spin octahedral Fe (III) with spectral parameters, including center shift (CS), quadrupole splitting (QS), and hyperfine magnetic field (H) values, which are consistent with those of pure bulk hematite (Table S2) (Larese-Casanova and Scherer, 2007a; Larese-Casanova and Scherer, 2007b). At 298 K, both types of hematite nanoparticles were determined to be fully in the weakly ferromagnetic (WF) state based on the single sextet with a QS of

about -0.20 mm·s^{-1} (Fig. S4) (Gee et al., 2004; Xu et al., 2015). However, at 13 K, the hematite nanoparticles were entirely antiferromagnetic (AF), and the QS values of HNCs and HNPs were 0.34 and 0.27 mm·s^{-1}, respectively. These QS values are the quadrupole moment of the state, which depends on the angle between the magnetic hyperfine field and the principal axis of the electric field gradient (Morrish, 1994; Long and Grandjean, 2013). The deviation of the QS value of the AF state indicates that the spin reorientations in HNCs and HNPs occurred from the basal plane toward directions of 26° and 28° relative to the *c*-axis, respectively, during the Morin transition corresponding to the [101] direction (Gee et al., 2004; Long and Grandjean, 2013; Kubaniova et al., 2019). The crystal facet is crucial in influencing the magnetic properties
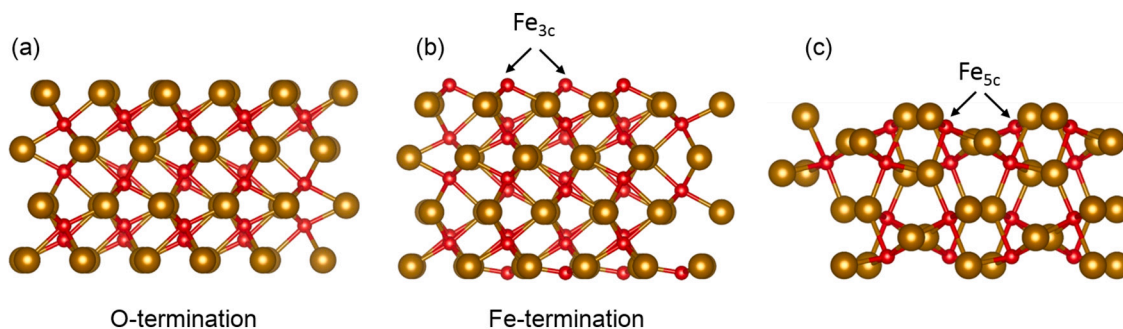
Fig. 2. Side views of surface terminations of hematite (Catalano et al., 2010). (a) O-termination of {001} facet, (b) Fe-termination of {001} facet, and {012} facet, Large yellow spheres are oxygen and small red spheres are iron. The under-coordinated Fe atoms on the {012} and {110} surfaces are shown by arrows, visualized using Vesta v.3.3.2 software (Momma and Izumi, 2011). (For interpretation of the references to colour in this figure legend, the reader is referred to the web version of this article.)
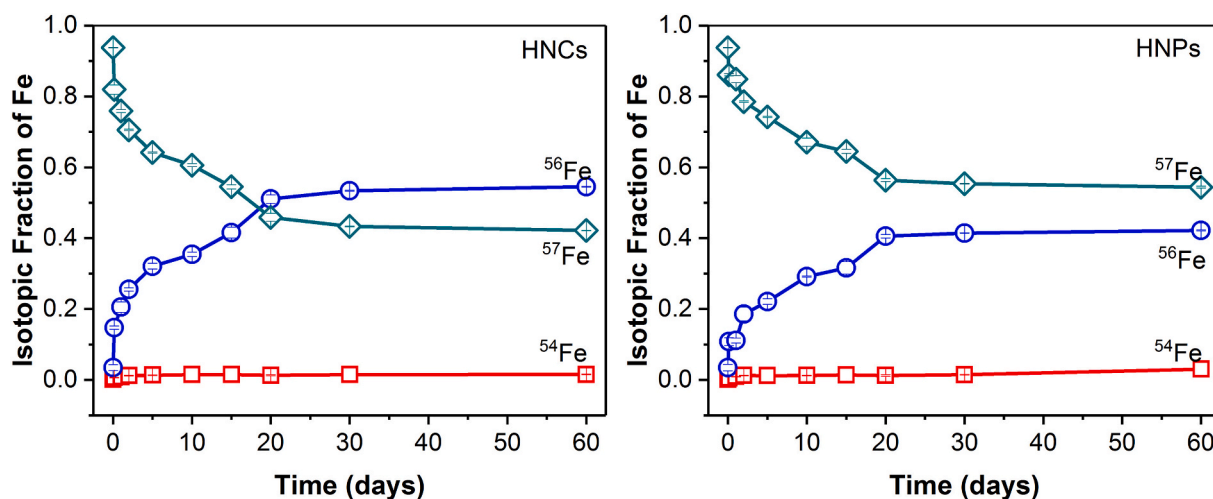
Fig. 3. Temporal evolution of the iron isotope fractions of Fe(II)$_{aq}$ during its reaction with HNCs and hematite{001} at pH 7.5. Aqueous Fe(II) was initially enriched in ^{57}Fe (~0.938), and hence depleted in ^{56}Fe (0.040) and ^{54}Fe (0.001). Hematite initially has a natural-abundance iron isotope composition (0.022, 0.917, and 0.058 for ^{57}Fe, ^{56}Fe, and ^{54}Fe, respectively). Reaction conditions: 1 mM aqueous Fe(II), 2 g·L^{-1} hematite, and 25 mM HEPES/KBr (pH 7.5). Values for data points represent the mean of duplicate reactions; error bars not visible are smaller than symbols.
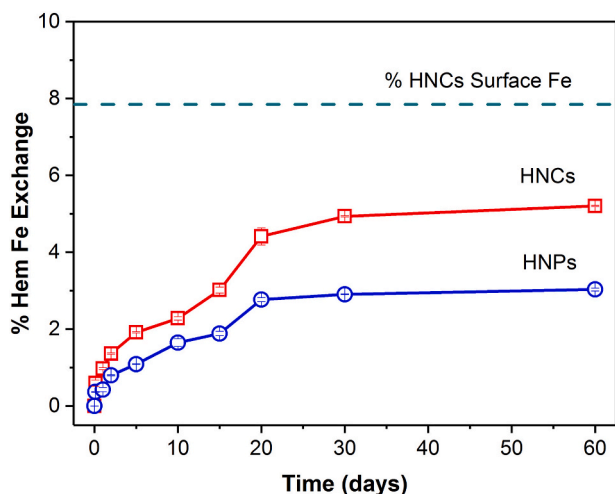
Fig. 4. Percent iron exchange over time for HNCs and HNPs. Dashed line is the percentage of iron atoms located at the surface of HNCs (See Text S4 for calculation). Values for data points represent the mean of duplicate reactions; error bars not visible are smaller than symbols.

of hematite nanocrystals (Chen et al., 2014). The differences in the magnetic properties of the studied HNCs and HNPs are primarily attributed to the distinct structural differences associated with the crystal facets of hematite nanoparticles.

3.2. Facet-specific isotope exchange between Fe(II)$_{aq}$ and hematite

The Fe(II)$_{aq}$ concentrations were measured at different time points after initiating the reaction between the Fe(II)$_{aq}$ and hematite. The concentration of Fe(II)$_{aq}$ decreased from 0.95 mM to 0.80 mM after 24 h, and then, it decreased further to 0.65 mM at 30 days and to 0.61 mM at 60 days (HNCs; Fig. S5). This gradual decrease in the Fe(II)$_{aq}$ concentration is consistent with previous studies conducted using goethite under similar experimental conditions (Frierdich et al., 2014; Alexandrov and Rosso, 2015; Joshi et al., 2017). This loss is due to the sorption of Fe(II) by the solid, accompanied by an increase in the concentration of Fe(II)$_{extr}$. The Fe(II) mass balance was greater than 95% for most of the experiments (Table S4), indicating that the 0.4 M HCl extraction efficiently recovered the majority of the associated Fe(II) but may not have captured the firmly bound or structurally incorporated Fe(II).

The time profile and corresponding simulated kinetic parameters demonstrate that the Fe(II) adsorption process conformed to the pseudo-initial kinetic equation. The adsorption capacities were obtained from the adsorption kinetic curves (Fig. S5). As revealed by Table 1, the Fe(II)
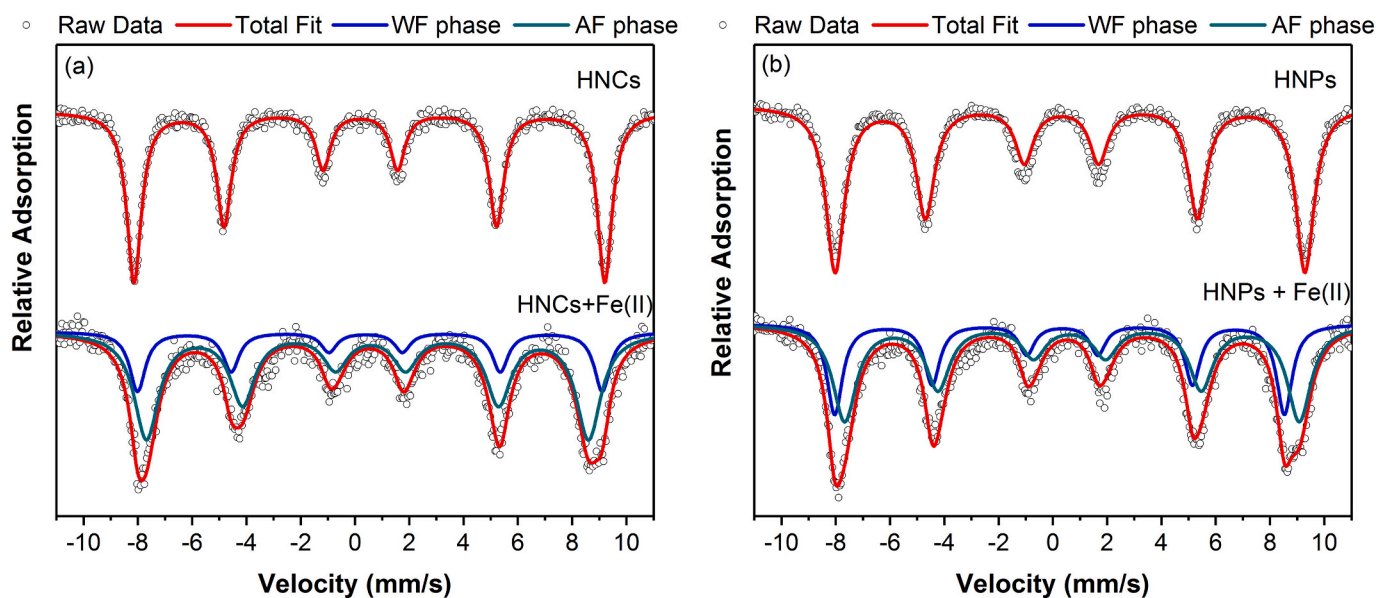
Fig. 5. Mössbauer spectra at 13 K of hematite before and after exposure to aqueous ^{57}Fe(II).

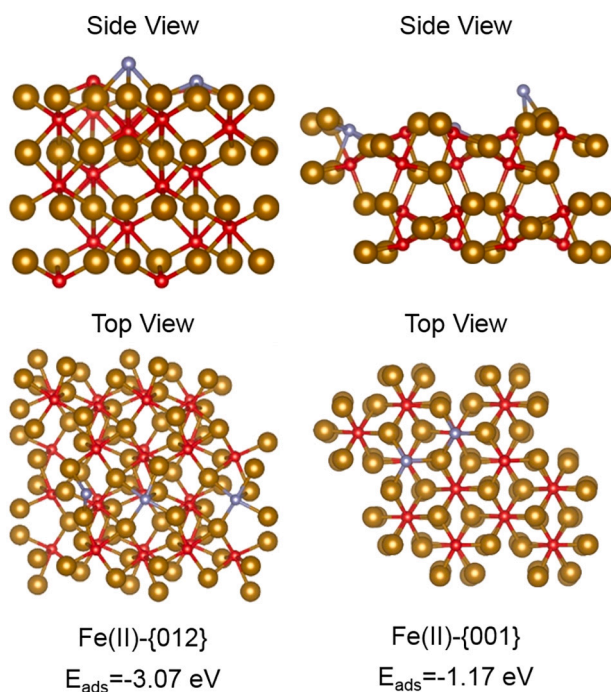**Fig. 6.** Schematic models illustrating the transformations of the {001}and {012}surfaces. Oxygen atoms are represented by red spheres, Fe(III) atoms are represented as yellow spheres, and Fe(II) oxidatively adsorbing on surface are represented as blue spheres. (For interpretation of the references to colour in this figure legend, the reader is referred to the web version of this article.)

adsorption capacities of HNCs and HNPs were 150.8 and 101.3 μmol·g^{-1}, respectively. The concentrations at which a monolayer of Fe formed on hematite surfaces can be estimated from the measured specific surface area (SSA) and the approximate sorption density. Assuming that the surface coverage was 2.5 sites·nm^{-2} (Jeon et al., 2001; Jeon et al., 2003), the values consistent with the average lattice Fe site densities and the monolayer coverage of HNCs and HNPs were estimated to be 169.0 and 171.5 μmol·g^{-1}, respectively. Thus, for the reacted hematite nanoparticles, on average, less than ~1 monolayer of Fe(II) was deposited on the surface. However, previous studies conducted using

hematite polycrystalline under similar experimental conditions found that the amount of sorbed Fe(II) exceeds the monolayer coverage (Frierdich et al., 2015; Larese-Casanova and Scherer, 2007a). A recent work has shown that the Fe(II) adsorption capability of goethite nanoparticles appear to be inversely proportional to the initial crystallinity of goethite (Southall et al., 2018). The low adsorptions observed in present study might be attributed to the high crystallinity of a single hematite crystal, which provides less active surface sites for the sorption of Fe(II) ions. In addition, the Fe(II) adsorption equilibrium was studied by using the Langmuir isotherm model and Freundlich isotherm model, respectively (Text S3 and Fig. S6) (Langmuir, 1916; Freundlich, 1928). The coefficient R^2 values in the Langmuir model were higher than those in the Freundlich model (Table S3), indicating that Fe(II) adsorption preferred monolayer adsorption. These results are in agreement with a previous study conducted on hematite polycrystalline samples under similar experimental conditions (Frierdich et al., 2015). In order to compare the Fe(II) adsorption capacities of the exposed facets of hematite, the amount of sorbed Fe(II) on the two samples were normalized by the surface areas. The normalized total site densities (Γ) were calculated to be 2.23 and 1.48 #Fe·nm^{-2} for HNCs and HNPs, respectively. Regarding the exposed facets of hematite, we subsequently estimated the iron species confined on the individual facets, which were 2.23 and 1.70 # Fe·nm^{-2} for the {012} and {001} facets of hematite, respectively (Table 1). Therefore, a higher density of Fe(II) can be adsorbed on the {012} facet than on the {001} facet of hematite. Since the atomic density of Fe on two facets is similar to each other, the different Fe(II) adsorption capacities of hematite facets may be due to their different reactive surface site densities or the different coordination modes of Fe(II) on hematite facets (Huang et al., 2016b; Yuan et al., 2017).

In addition to the Fe(II) concentrations, the Fe isotopic compositions of all three Fe fractions (i.e., Fe(II)$_{aq}$, Fe(II)$_{extr}$, hematite) changed throughout the reaction (Fig. 3). The fraction of ^{57}Fe in the Fe(II)$_{aq}$ decreased from 0.94 to 0.42 after 60 days (HNCs), whereas the amounts of ^{56}Fe and ^{54}Fe in the aqueous phase increased toward the system's mass balance (Fig. 3 and Table S4). These results indicate that some of the ^{57}Fe in the aqueous Fe(II) had been replaced with ^{56}Fe and ^{54}Fe atoms from the structural Fe(III) in hematite. The calculations of the percent iron exchange in hematite, via f ^{57}Fe of Fe(II)$_{aq}$ (Eq. 1), reveal that substantially different amounts of exchange occurred for HNCs and HNPs, i.e., 5.2% and 3.0%, respectively (Fig. 4). By using the SSA of each

particle size and the available crystallographic information to determine the surface site density (Southall et al., 2018), the percentages of the Fe atoms on the surfaces of the HNCs and HNPs were calculated to be 7.9% and 7.7%, respectively (see SI Text S4 for calculations). These results suggest that the initial crystallite size of the minerals or the amount of surface atoms does not affect the observed differences in the extent of Fe atom exchange, and several other factors control the electron transfer between the Fe(II)$_{aq}$ and hematite. Considering the high dispersity and crystallinity of HNCs and HNPs (Fig. 1 and Fig. S3), as well as their similar specific surface areas (Table 1), it is conceivable that the differences observed in the adsorption capacity of Fe(II)$_{aq}$ and the extent of hematite recrystallization are depend on the exposed facets hematite. Specifically, the exposed facets of hematite must contain different numbers of surface active sites and/or binding energies to manifest variable adsorption capacities between particles with the same underlying chemical composition, which further affects the Fe atom exchange capacity. Given the specific facet expression of HNCs versus HNPs, this suggests that {012} facets own more active sites for electron accepting, and is more favorable for electron transfer from Fe(II) to its surface.

3.3. Structural variations and magnetic changes of hematite single crystals after reaction with Fe(II)$_{aq}$

To determine whether the mineral structure and magnetic property change during the course of the Fe(II)-catalyzed recrystallization, we characterized hematite nanoparticles after the reaction using XRD, HR-TEM, and Mössbauer spectroscopy. The XRD patterns of both types of hematite nanoparticles after reaction with Fe(II)$_{aq}$ did not show the formation of new iron mineral phases (Fig. S7). Therefore, the Fe atom exchange that we observed (Fig. 3) does not involve a mineralogical transformation. Although both materials were mineralogically pure at the resolution of the XRD instrument, there were subtle changes in the positions of the peaks (Fig. S8). The diffraction peaks gradually shifted to lower angles, especially the (104) and (110) peaks. This indicates that the d-spacings of these planes increased after the reaction with Fe(II)$_{aq}$, suggesting lattice contraction during the substitution of Fe(II) for the lattice Fe(III) in the hematite crystals (Li et al., 2016; Jiang et al., 2020). In contrast, after 30 days, the XRD pattern of the hematite nanoparticles in the control experiment without Fe(II)$_{aq}$ were indistinguishable from that before reaction (Fig. S7). Rietveld structure refinements of these samples were also conducted, and the results are presented in Fig. S7 and Table S5. The unit cell parameters *a* and *c* increased for both types of hematite nanoparticles after reaction with Fe(*II*)$_{aq}$, in which the crystallite sizes of the HNCs and HNPs increased by 3.1% and 2.6%, respectively (Table S5). These increases in the hematite crystallite sizes during the reaction with Fe(II)$_{aq}$ are attributed to particle coarsening through Ostwald ripening (Southall et al., 2018), which has also been observed during epsomite (Li et al., 2011), calcite (Heberling et al., 2016), and barite (Heberling et al., 2018) recrystallization.

Such increases in crystallite size may be visible through detailed microscopic analysis, and thus, we examined the hematite nanoparticles using HR-TEM. The HR-TEM images of hematite nanoparticles before and after the reaction showed that no new phases were present after the reaction with Fe(II)$_{aq}$ (Fig. S9). Furthermore, qualitative differences in the particle aggregates and individual particles were not detected, and no indication of preferential growth or dissolution on specific crystal facets were observed. Similar results were observed for goethite and hematite polycrystalline samples (Handler et al., 2014; Frierdich et al., 2015), in which the particles appeared unmodified in terms of these characteristics despite the Fe atom exchange that occurred. Our observations are consistent with the XRR measurements, that is, the reacted hematite surfaces maintained their long-range crystallographic order and structural identity even in the uppermost surface planes (Catalano et al., 2010). For example, the atomic-scale structural analysis of reacted HNPs with Cs-corrected scanning transmission electron microscopy (STEM) exhibited flat surface and a clear lattice fringe, indicating that

the atoms were well arranged at the basal surfaces and edges (Fig. S9d). These results indicate that the oxidation of the Fe(II) and the growth of the newly formed hematite crystallites on the hematite surface was an epitaxial extension of the underlying hematite lattice.

To examine whether the Fe(II)–Fe(III) interfacial electron transfer induces electronic or magnetic changes in the bulk hematite, the ^{57}Fe Mössbauer spectra of hematite after the reaction were obtained at 13 K. The ^{57}Fe Mössbauer spectra confirm that no new phases emerged during the reaction with Fe(II)$_{aq}$ (Fig. 5), and no Fe(II) was observed in the reacted hematite samples. This is likely due to the fast valence electron transfer rate between the adsorbed Fe(II) and the Fe(III) atoms in hematite (Rosso et al., 2003; Larese-Casanova and Scherer, 2007b). Although both materials were mineralogically pure, the reacted hematite exhibited a markedly different magnetic behavior compared to bulk ^{NA}hematite. Unlike the unreacted hematite nanoparticles that only have one sextet at 13 K (Fig. S4), the spectra of the reacted hematite samples contain two distinct sextets (Fig. 5), representing the Fe in the different magnetic domains, i.e., the AF phase and WF phase, which are clearly distinguishable based on their quadrupole splitting distributions (Table S6). The coexistence of the AF and WF phases in the reacted hematite samples at 13 K indicates that the Morin Transition was suppressed, and the magnetic properties of reacted hematite were different from pure, bulk hematite. The control experiments without ^{57}Fe(II)$_{aq}$ showed no suppression of the Morin transition (data not shown), indicating that the suppression was due to the exposure to Fe(II)$_{aq}$ rather than the hydration of hematite surface or interactions with the other ions in the reaction system. The suppression of the Morin transition during Fe(II)-catalyzed hematite recrystallization was caused by the spin-orbit coupling due to the Fe(II) doping and the larger Fe(II) radius (0.76 A vs 0.64 A for Fe(III)) (Morrish, 1994; Larese-Casanova and Scherer, 2007a; Larese-Casanova and Scherer, 2007b; Rosso et al., 2010).

Both HNCs and HNPs underwent Morin transition suppression after the reaction, but their suppression extents were significantly different. As is illustrated in Fig. 5 and Table S6, the WF phase abundances of the HNCs and HNPs at 13 K after reaction with Fe(II)$_{aq}$ were ~ 73.6% and ~ 38.0% (based on the spectra areas), respectively. The large percentage of iron atoms affected is consistent with theoretical calculations, which indicates that the donated electrons from sorbed Fe(II) are readily delocalized and rapidly transferred within the hematite lattice and affect several Fe atoms (Kerisit and Rosso, 2006). In addition, a small amount of Fe(II) doping in hematite can significantly suppress the Morin transition (Morrish, 1994), and the degree of Morin transition suppression of hematite was positively correlated with the amount of Fe(II) doping (Larese-Casanova and Scherer, 2007b). Therefore, the higher suppression of the Morin transition for hematite {012} may resulted from the larger amount of Fe(II) adsorbed (Table 1). It should be noted that the ^{57}Fe in the original bulk hematite (of natural isotopic abundance) occupies a considerable proportion of the total ^{57}Fe in the reacted samples, and may migrate to the surface or near-surface of hematite, thus having a significant dopant effect on the Morin transition.

3.4. Mechanisms of the facet-specific reactivity of hematite

The above isotope experiments and structural characterization results clearly show the preferential adsorption of Fe(II) on the {012} facet compared to the {001} facet of hematite at a circumneutral pH. In addition, HNCs underwent more Fe atom exchange and magnetic changes. It is well known that the reactivity of a mineral is determined by the atomic arrangement of its surface (Hoffmann et al., 1995). In the hematite structure, each Fe atom has six nearest neighbor O ions, comprising a FeO$_6$ octahedron. Each FeO$_6$ octahedron shares edges with three neighboring octahedrons in the same plane and shares a face with one octahedron in the adjacent plane (Huang et al., 2016b). Therefore, the coordination environment of the surface Fe is differentiated on the various exposed facets, such as the {001} and {012} facets of the studied

hematite crystallites.

Previous theoretical and experimental results suggest that the density of the under-coordinated surface Fe(III) cations has an important influence on the adsorption capacity of minerals (Venema et al., 1998; Huang et al., 2017a; Yan et al., 2020). Therefore, to further understand how the exposed facets of hematite affect the adsorption of Fe(II), we performed DFT calculations to explore the adsorption structures and energies of Fe(II) on hematite surfaces. The atomic arrangements of hematite in side view are shown in Fig. 6. The {012} hematite facet exhibits a unique ridge-and-valley topography of 5-fold under-coordinated Fe surface sites (Fig. 6) (Catalano et al., 2007; Zhou et al., 2012). The existence of surface Fe_{5c} sites gives the {012} facet a typical polar surface (Rustad et al., 1999; Vohs, 2013), making the {012} facet favors the protonation and deprotonation reactions for charge accumulation. When Fe(II) comes into contact with Fe(II)$_{aq}$, the surface Fe_{5c} sites are modified via the adsorption of Fe(II) by hematite to confine the Fe(II) on the surface in a 5-coordination mode (Fig. 6). This 5-coordination binding mode was confirmed by the layer-by-layer growth on the {012} surface (Catalano et al., 2010). In contrast, the {001} facets can form O- or Fe-terminated surfaces (Fig. 4a); and the Fe-termination was demonstrated to be the stable mode according to previous experimental and theoretical studies (Trainor et al., 2004; Liu et al., 2016). The Fe-terminated HNPs facets have a single iron-layer with 100% 3-fold under-coordinated Fe surface sites. When the {001} facet comes into contact with Fe(II)$_{aq}$, the coexisting structural domains are modified via the adsorption of Fe(II), resulting in 6-coordinated Fe(II) being adsorbed onto the surface (Fig. 6). This 6-coordination binding mode was confirmed by the nucleation of islands on the {001} surface (Rosso et al., 2010). Therefore, we conclude that the 5-coordination binding mode of Fe(II) confined on the {012} facet benefits charge accumulation and electron transfer more than the 6-coordination binding mode on the {001} facet.

Moreover, the particular topography of the {012} facet exposes a greater number of under-coordinated surface iron cations than the {001} facet (Zhou et al., 2012). The densities of the under-coordinated iron cation-active sites on the {012} and {001} facets were estimated to be 7.3 and 4.6 atoms·nm^{-2}, respectively (Table S7). Unlike bulk Fe cations, which are octahedrally coordinated with 6 O anions, the under-coordinated Fe cations provide adsorption active sites for Fe(II). The bond valence calculation and surface complexation model of the ideal structure of the hematite surface terminations generally infers a higher binding affinity on surfaces with more under-coordinated surface ligands (Venema et al., 1998). Moreover, molecular dynamics simulations have shown that Fe(II) sorption onto one idealized {001} termination is dominated by weak outer-sphere binding (Kerisit et al., 2015). Based on these surface atomic arrangements, DFT calculations were also performed to explore the adsorption structures and adsorption energies (Eads) of Fe(II) on the different facets of hematite. The E$_{ads}$ of the {012} and {001} facets for Fe(II) adsorption were $-$ 3.07 and $-$ 1.17 eV, respectively (Table S7). The more negative Eads for Fe(II) on the {012} facet suggests that HNCs has a higher adsorption capability for Fe(II) than HNPs, which may explain the different adsorption performances observed in our experiments (Fig. S5).

Our findings also reveal that HNCs underwent more Fe atom exchange than HNPs. The differences in the extent of the Fe atom exchange are mainly ascribed to two factors: the adsorption capacity and the electron transfer reactivity on the two facets (Larese-Casanova and Scherer, 2007a). First, since more Fe(II) adsorbs onto the HNCs, there is a higher probability of Fe(II)-hematite interfacial complexes forming, which leads to a more efficient exchange of Fe atoms. Second, the electrostatic potentials measured for the individual facets suggest that the {012} facets electrostatically outcompete for Fe(II) with the {001} facets (Tanwar et al., 2008; Chatman et al., 2013). In addition, the {001} facet is relatively inert to the protonation and deprotonation reactions for charge accumulation due to its nonpolar surface characteristic (Eggleston et al., 2003; Vohs, 2013). Consequently, electron transfer is

more favorable on the {012} facet than on the {001} facet, and HNCs can undergo more Fe atom exchange than HNPs. Overall, the results of the kinetics experiments and structural analyses preformed in this study provide in-depth knowledge of the interfacial interactions between Fe (II) and hematite with different exposed facets during Fe(II)$_{aq}$-catalyzed recrystallization.

4. Conclusions

The results of the present study demonstrated the importance of crystal morphology in Fe(II)$_{aq}$-catalyzed recrystallization process. Batch experiments results indicated HNCs adsorbed more Fe(II) and underwent higher efficient Fe atom exchange than HNPs. The deference in the adsorption capacity and Fe atom exchange of these specific faceted nanocrystals were ascribed to the density of unsaturated Fe cations and their coordination environments. Based on the DFT calculations, the adsorption energy for the adsorption of Fe(II) on {012} facet (-3.07 eV) was lower than that (-1.17 eV) of {001} facet, resulted in better adsorption capacity of HNCs than that of HNPs. In addition, Mössbauer spectra analysis showed that both reacted hematite nanoparticles underwent Morin transition suppression, and the abundances of the WF phase at 13 K of HNCs and HNPs after reaction with Fe(II)$_{aq}$ were ~ 73.6% and ~ 38.0%, respectively. The findings of this study support the hypothesis that adsorption capacity and mechanism of hematite are contingent on the individual facets and further contingent on surface sites (Cornell and Schwertmann, 2003). The mechanistic insights into facet-dependent Fe atom exchange of hematite would improve our understanding on the basic mechanism and key factors during the Fe(II)-catalyzed recrystallization of iron (hydr)oxides in natural environments.

Declaration of interests

The authors declare that they have no known competing financial interests or personal relationships that could have appeared to influence the work reported in this paper.

Declaration of Competing Interest

The authors declare that they have no known competing financial interests or personal relationships that could have appeared to influence the work reported in this paper.

Appendix A. Supplementary data

Supplementary data to this article can be found online at https://doi.org/10.1016/j.chemgeo.2021.120460.

References

Alexandrov, V., Rosso, K.M., 2015. Ab initio modeling of Fe(II) adsorption and interfacial electron transfer at goethite (α-FeOOH) surfaces. Phys. Chem. Chem. Phys. 17 (22), 14518–14531.

Baltrusaitis, J., Cwiertny, D.M., Grassian, V.H., 2007. Adsorption of sulfur dioxide on hematite and goethite particle surfaces. Phys. Chem. Chem. Phys. 9 (41), 5542–5554.

Cao, S., Zhang, X., Huang, X., Wan, S., An, X., Jia, F., Zhang, L., 2019. Insights into the facet-dependent adsorption of phenylarsonic acid on hematite nanocrystals. Environ. Sci. Nano 6 (11), 3280–3291.

Carbone, C., Di Benedetto, F., Marescotti, P., Martinelli, A., Sangregorio, C., Cipriani, C., Lucchetti, G., Romanelli, M., 2005. Genetic evolution of nanocrystalline Fe oxide and oxyhydroxide assemblages from the Libiola mine (eastern Liguria, Italy): structural and microstructural investigations. Eur. J. Mineral. 17 (5), 785–795.

Catalano, J.G., Fenter, P., Park, C.J., 2007. Interfacial water structure on the (012) surface of hematite: ordering and reactivity in comparison with corundum. Geochim. Cosmochim. Acta 71 (22), 5313–5324.

Catalano, J.G., Fenter, P., Park, C., Zhang, Z., Rosso, K.M., 2010. Structure and oxidation state of hematite surfaces reacted with aqueous Fe(II) at acidic and neutral pH. Geochim. Cosmochim. Acta 74 (5), 1498–1512.

Chan, J.Y., Ang, S.Y., Ye, E.Y., Sullivan, M., Zhang, J., Lin, M., 2015. Heterogeneous photo-Fenton reaction on hematite (α-Fe$_2$O$_3$) {104}, {113} and {001} surface facets. Phys. Chem. Chem. Phys. 17 (38), 25333–25341.

Chatman, S., Zarzycki, P., Rosso, K.M., 2013. Surface potentials of (001), (012), (113) hematite (α-Fe$_2$O$_3$) crystal faces in aqueous solution. Phys. Chem. Chem. Phys. 15 (33), 13911–13921.

Chen, L., Yang, X., Chen, J., Liu, J., Wu, H., Zhan, H., Liang, C., Wu, M., 2010. Continuous shape- and spectroscopy-tuning of hematite nanocrystals. Inorg. Chem. 49 (18), 8411–8420.

Chen, J.S., Chen, X., Li, Y., Chen, X., Ramanujan, R.V., Hu, X., 2014. Distinct optical and magnetic properties of ionic liquid tuned hematite nanocrystals having different exposed (001) facets. RSC Adv. 4 (2), 593–597.

Cornell, R.M., Schwertmann, U., 2003. The Iron Oxides: Structure, Properties, Reactions, Occurrences and Uses. John Wiley & Sons.

Descostes, M., Mercier, F., Thromat, N., Beaucaire, C., Gautier-Soyer, M., 2000. Use of XPS in the determination of chemical environment and oxidation state of iron and sulfur samples: constitution of a data basis in binding energies for Fe and S reference compounds and applications to the evidence of surface species of an oxidized pyrite in a carbonate medium. Appl. Surf. Sci. 165 (4), 288–302.

Echigo, T., Monsegue, N., Aruguete, D.M., Murayama, M., Hochella, M.F., 2012. Nanopores in hematite (α-Fe$_2$O$_3$) nanocrystals observed by electron tomography. Am. Mineral. 98 (1), 154–162.

Eggleston, C.M., Stack, A.G., Rosso, K.M., Higgins, S.R., Bice, A.M., Boese, S.W., Pribyl, R.D., Nichols, J., 2003. The structure of hematite (α-Fe$_2$O$_3$)(001) surfaces in aqueous media: Scanning tunneling microscopy and resonant tunneling calculations of coexisting O and Fe terminations. Geochim. Cosmochim. Acta 67 (5), 985–1000.

Freundlich, H., 1928. Colloid and Capillary. E. P. Dutton and Co., New York.

Frierdich, A.J., Beard, B.L., Reddy, T.R., Scherer, M.M., Johnson, C.M., 2014. Iron isotope fractionation between aqueous Fe(II) and goethite revisited: New insights based on a multi-direction approach to equilibrium and isotopic exchange rate modification. Geochim. Cosmochim. Acta 139, 383–398.

Frierdich, A.J., Helgeson, M., Liu, C., Wang, C., Rosso, K.M., Scherer, M.M., 2015. Iron atom exchange between hematite and aqueous Fe(II). Environ. Sci. Technol. 49 (14), 8479–8486.

Gee, S.H., Hong, Y.K., Sur, J.C., Erickson, D.W., Park, M.H., Jeffers, F., 2004. Spin orientation of hematite (α-Fe$_2$O$_3$) nanoparticles during the Morin transition. IEEE Trans. Magn. 40 (4), 2691–2693.

Guo, T., Jiang, L., Wang, K., Li, Y., Huang, H., Wu, X., Zhang, G., 2021. Efficient persulfate activation by hematite nanocrystals for degradation of organic pollutants under visible light irradiation: Facet-dependent catalytic performance and degradation mechanism. Appl. Catal. B 286, 119883.

Handler, R.M., Beard, B.L., Johnson, C.M., Scherer, M.M., 2009. Atom exchange between aqueous Fe(II) and goethite: an Fe isotope tracer study. Environ. Sci. Technol. 43 (4), 1102–1107.

Handler, R.M., Frierdich, A.J., Johnson, C.M., Rosso, K.M., Beard, B.L., Wang, C., Latta, D.E., Neumann, A., Pasakarnis, T., Premaratne, W.A., Scherer, M.M., 2014. Fe (II)-catalyzed recrystallization of goethite revisited. Environ. Sci. Technol. 48 (19), 11302–11311.

Heberling, F., Paulig, L., Nie, Z., Schild, D., Finck, N., 2016. Morphology controls on calcite recrystallization. Environ. Sci. Technol. 50 (21), 11735–11741.

Heberling, F., Metz, V., Böttle, M., Curti, E., Geckeis, H., 2018. Barite recrystallization in the presence of ^{226}Ra and ^{133}Ba. Geochim. Cosmochim. Acta 232, 124–139.

Hoffmann, M.R., Martin, S.T., Choi, W.Y., Bahnemann, D.W., 1995. Environmental applications of semiconductor photocatalysis. Chem. Rev. 95 (1), 69–96.

Huang, X., Hou, X., Song, F., Zhao, J., Zhang, L., 2016a. Facet-dependent Cr(VI) adsorption of hematite nanocrystals. Environ. Sci. Technol. 50 (4), 1964–1972.

Huang, X., Hou, X., Zhao, J., Zhang, L., 2016b. Hematite facet confined ferrous ions as high efficient Fenton catalysts to degrade organic contaminants by lowering H$_2$O$_2$ decomposition energetic span. Appl. Catal. B 181, 127–137.

Huang, X., Hou, X., Jia, F., Song, F., Zhao, J., Zhang, L., 2017a. Ascorbate-promoted surface iron cycle for efficient heterogeneous Fenton alachlor degradation with hematite nanocrystals. ACS Appl. Mater. Interfaces 9 (10), 8751–8758.

Huang, X., Hou, X., Song, F., Zhao, J., Zhang, L., 2017b. Ascorbate induced facet dependent reductive dissolution of hematite nanocrystals. J. Phys. Chem. C 121 (2), 1113–1121.

Huang, X., Chen, Y., Walter, E., Zong, M., Wang, Y., Zhang, X., Qafoku, O., Wang, Z., Rosso, K.M., 2019a. Facet-specific photocatalytic degradation of organics by heterogeneous Fenton chemistry on hematite nanoparticles. Environ. Sci. Technol. 53 (17), 10197–10207.

Huang, X., Hou, X., Wang, F., Guo, B., Song, F., Ling, L., Zhao, J., Zhang, L., 2019b. Molecular-scale structures of uranyl surface complexes on hematite facets. Environ. Sci. Nano 6 (3), 892–903.

Jeon, B.-H., Dempsey, B.A., Burgos, W.D., Royer, R.A., 2001. Reactions of ferrous iron with hematite. Colloids Surf. A Physicochem. Eng. Asp. 191 (1–2), 41–55.

Jeon, B.-H., Dempsey, B.A., Burgos, W.D., Royer, R.A., 2003. Sorption kinetics of Fe(II), Zn(II), Co(II), Ni(II), Cd(II), and Fe(II)/Me(II) onto hematite. Water Res. 37 (17), 4135–4142.

Jiang, S., Yan, X., Peacock, C.L., Zhang, S., Li, W., Zhang, J., Feng, X., Liu, F., Yin, H., 2020. Adsorption of Cr(VI) on Al-substituted hematites and its reduction and retention in the presence of Fe^{2+} under conditions similar to subsurface soil environments. J. Hazard. Mater. 390, 122014.

Jordan, D.S., Hull, C.J., Troiano, J.M., Riha, S.C., Martinson, A.B.F., Rosso, K.M., Geiger, F.M., 2013. Second harmonic generation studies of Fe(II) interactions with hematite (α-Fe$_2$O$_3$). J. Phys. Chem. C 117 (8), 4040–4047.

Joshi, P., Gorski, C.A., 2016. Anisotropic morphological changes in goethite during Fe^{2+}-catalyzed recrystallization. Environ. Sci. Technol. 50 (14), 7315–7324.

Joshi, P., Fantle, M.S., Larese-Casanova, P., Gorski, C.A., 2017. Susceptibility of goethite to Fe^{2+}-catalyzed recrystallization over Time. Environ. Sci. Technol. 51 (20), 11681–11691.

Kerisit, S., Rosso, K.M., 2006. Computer simulation of electron transfer at hematite surfaces. Geochim. Cosmochim. Acta 70 (8), 1888–1903.

Kerisit, S., Zarzycki, P., Rosso, K.M., 2015. Computational molecular simulation of the oxidative adsorption of ferrous iron at the hematite (001)–water interface. J. Phys. Chem. C 119 (17), 9242–9252.

Kubaniova, D., Kubickova, L., Kmjec, T., Zaveta, K., Niznansky, D., Brazda, P., Klementova, M., Kohout, J., 2019. Hematite: Morin temperature of nanoparticles with different size. J. Magn. Magn. Mater. 475, 611–619.

Langmuir, I., 1916. The constitution and fundament properties of solids and liquids. Part 1. Solids. J. Am. Chem. Soc. 38, 2221–2295.

Larese-Casanova, P., Scherer, M.M., 2007a. Fe(II) sorption on hematite: new insights based on spectroscopic measurements. Environ. Sci. Technol. 41 (2), 471–477.

Larese-Casanova, P., Scherer, M.M., 2007b. Morin transition suppression in Polycrystalline ^{57}Hematite (α-Fe$_2$O$_3$) exposed to ^{56}Fe(II). Hyperfine Interact 174 (1–3), 111–119.

Li, W.Q., Beard, B.L., Johnson, C.M., 2011. Exchange and fractionation of Mg isotopes between epsomite and saturated MgSO$_4$ solution. Geochim. Cosmochim. Acta 75 (7), 1814–1828.

Li, W., Liang, X., An, P., Feng, X., Tan, W., Qiu, G., Yin, H., Liu, F., 2016. Mechanisms on the morphology variation of hematite crystals by Al substitution: the modification of Fe and O reticular densities. Sci. Rep. 6, 35960.

Li, T., Zhong, W., Jing, C., Li, X., Zhang, T., Jiang, C., Chen, W., 2020. Enhanced hydrolysis of p-nitrophenyl phosphate by iron (hydr)oxide nanoparticles: roles of exposed facets. Environ. Sci. Technol. 54 (14), 8658–8667.

Liang, Y., Wang, M., Xiong, J., Hou, J., Wang, X., Tan, W., 2019. Al-substitution-induced defect sites enhance adsorption of Pb^{2+} on hematite. Environ. Sci. Nano 6 (5), 1323–1331.

Liu, T., Xue, L., Guo, X., Huang, Y., Zheng, C., 2016. DFT and experimental study on the mechanism of elemental mercury capture in the presence of HCl on α-Fe$_2$O$_3$ (001). Environ. Sci. Technol. 50 (9), 4863–4868.

Long, G.J., Grandjean, F., 2013. Mössbauer Spectroscopy Applied to Magnetism and Materials Science, 1. Springer Science & Business Media.

Lounsbury, A.W., Wang, R., Plata, D.L., Billmeyer, N., Muhich, C., Kanie, K., Sugimoto, T., Peak, D., Zimmerman, J.B., 2019. Preferential adsorption of selenium oxyanions onto {110} and {012} nano-hematite facets. J. Colloid Interface Sci. 537, 465–474.

Lv, J., Miao, Y., Huang, Z., Han, R., Zhang, S., 2018. Facet-mediated adsorption and molecular fractionation of humic substances on hematite surfaces. Environ. Sci. Technol. 52 (20), 11660–11669.

Mackrodt, W.C., Davey, R.J., Black, S.N., Docherty, R., 1987. The morphology of α-Al$_2$O$_3$ and α-Fe$_2$O$_3$: the importance of surface relaxation. J. Cryst. Growth 80 (2), 441–446.

Mei, H., Liu, Y., Tan, X., Feng, J., Ai, Y., Fang, M., 2020. U(VI) adsorption on hematite nanocrystals: Insights into the reactivity of {001} and {012} facets. J. Hazard. Mater. 399, 123028.

Momma, K., Izumi, F., 2011. VESTA 3 for three-dimensional visualization of crystal, volumetric and morphology data. J. Appl. Crystallogr. 44 (6), 1272–1276.

Morrish, A.H., 1994. Canted Antiferromagnetism: Hematite. World Scientific.

Noerpel, M.R., Lee, S.S., Lenhart, J.J., 2016. X-ray analyses of Lead adsorption on the (001), (110), and (012) hematite surfaces. Environ. Sci. Technol. 50 (22), 12283–12291.

Norgren, B., Somers, M., De Wit, J., 1994. Application of tougaard background subtraction to XPS spectra of passivated Fe–17 Cr. Surf. Interface Anal. 21 (6–7), 378–381.

Notini, L., Latta, D.E., Neumann, A., Pearce, C.I., Sassi, M., N'Diaye, A.T., Rosso, K.M., Scherer, M.M., 2018. The Role of defects in Fe(II)-goethite electron transfer. Environ. Sci. Technol. 52 (5), 2751–2759.

Notini, L., Byrne, J.M., Tomaszewski, E.J., Latta, D.E., Zhou, Z., Scherer, M.M., Kappler, A., 2019. Mineral Defects Enhance Bioavailability of Goethite toward Microbial Fe(III) reduction. Environ. Sci. Technol. 53 (15), 8883–8891.

Ouyang, J., Pei, J., Kuang, Q., Xie, Z., Zheng, L., 2014. Supersaturation-controlled shape evolution of α-Fe$_2$O$_3$ nanocrystals and their facet-dependent catalytic and sensing properties. ACS Appl. Mater. Interfaces 6 (15), 12505–12514.

Qu, J., Yu, Y., Cao, C.Y., Song, W.G., 2013. α-Fe$_2$O$_3$ nanodisks: layered structure, growth mechanism, and enhanced photocatalytic property. Chem. Eur. J. 19 (34), 11172–11177.

Rosso, K.M., Smith, D.M.A., Dupuis, M., 2003. An ab initio model of electron transport in hematite (α-Fe$_2$O$_3$) basal planes. J. Chem. Phys. 118 (14), 6455–6466.

Rosso, K.M., Yanina, S.V., Gorski, C.A., Larese-Casanova, P., Scherer, M.M., 2010. Connecting observations of hematite (α-Fe$_2$O$_3$) growth catalyzed by Fe(II). Environ. Sci. Technol. 44 (1), 61–67.

Rustad, J.R., Wasserman, E., Felmy, A.R., 1999. Molecular modeling of the surface charging of hematite: II. Optimal proton distribution and simulation of surface charge versus pH relationships. Surf. Sci. 424 (1), 28–35.

Southall, S.C., Micklethwaite, S., Wilson, S.A., Frierdich, A.J., 2018. Changes in crystallinity and tracer-isotope distribution of goethite during Fe(II)-accelerated recrystallization. ACS Earth Space Chem. 2 (12), 1271–1282.

Stookey, L.L., 1970. Ferrozine—a new spectrophotometric reagent for iron. Anal. Chem. 42 (7), 779–781.

Sun, L., Zhan, W., Li, Y.-A., Wang, F., Zhang, X., Han, X., 2018. Understanding the facet-dependent catalytic performance of hematite microcrystals in a CO oxidation reaction. Inorg. Chem. Front. 5 (9), 2332–2339.

Tanwar, K.S., Petitto, S.C., Ghose, S.K., Eng, P.J., Trainor, T.P., 2008. Structural study of Fe (II) adsorption on hematite (1102). Geochim. Cosmochim. Acta 72 (14), 3311–3325.

Tanwar, K.S., Petitto, S.C., Ghose, S.K., Eng, P.J., Trainor, T.P., 2009. Fe(II) adsorption on hematite (0001). Geochim. Cosmochim. Acta 73 (15), 4346–4365.

Trainor, T.P., Chaka, A.M., Eng, P.J., Newville, M., Waychunas, G.A., Catalano, J.G., Brown, G.E., 2004. Structure and reactivity of the hydrated hematite (0001) surface. Surf. Sci. 573 (2), 204–224.

Venema, P., Hiemstra, T., Weidler, P.G., van Riemsdijk, W.H., 1998. Intrinsic proton affinity of reactive surface groups of metal (hydr)oxides: Application to iron (hydr) oxides. J. Colloid Interface Sci. 198 (2), 282–295.

Vohs, J.M., 2013. Site requirements for the adsorption and reaction of oxygenates on metal oxide surfaces. Chem. Rev. 113 (6), 4136–4163.

Wang, S.B., Min, Y.L., Yu, S.H., 2007. Synthesis and magnetic properties of uniform hematite nanocubes. J. Phys. Chem. C 111 (9), 3551–3554.

Xu, S., Habib, A.H., Gee, S.H., Hong, Y.K., McHenry, M.E., 2015. Spin orientation, structure, morphology, and magnetic properties of hematite nanoparticles. J. Appl. Phys. 117 (17).

Yan, L., Chan, T., Jing, C., 2020. Arsenic adsorption on hematite facets: spectroscopy and DFT study. Environ. Sci. Nano. 7 (12), 3927–3939.

Yanina, S.V., Rosso, K.M., 2008. Linked reactivity at mineral-water interfaces through bulk crystal conduction. Science 320 (5873), 218–222.

Yuan, Q., Li, P., Liu, J., Lin, Y., Cai, Y., Ye, Y., Liang, C., 2017. Facet-dependent selective adsorption of Mn-doped α-Fe$_2$O$_3$ nanocrystals toward heavy-metal ions. Chem. Mater. 29 (23), 10198–10205.

Zhou, X., Yang, H., Wang, C., Mao, X., Wang, Y., Yang, Y., Liu, G., 2010. Visible light induced photocatalytic degradation of rhodamine B on one-dimensional iron oxide particles. J. Phys. Chem. C 114 (40), 17051–17061.

Zhou, X., Lan, J., Liu, G., Deng, K., Yang, Y., Nie, G., Yu, J., Zhi, L., 2012. Facet-mediated photodegradation of organic dye over hematite architectures by visible light. Angew. Chem. Int. Ed. 51 (1), 178–182.

Zong, M., Song, D., Zhang, X., Huang, X., Lu, X., Rosso, K.M., 2021. Facet-dependent photodegradation of methylene blue by hematite nanoplates in visible light. Environ. Sci. Technol. 55 (1), 677–688.